Check for updates

ChemCatChem

Research Article
doi.org/10.1002/cctc.202500506

Chemistry Europe
European Chemical Societies Publishing

www.chemcatchem.org

Activity Boost for Cobalt–Selectivity Shift and Activation During CO_2 Methanation by Carbon Nitride-Modified Al_2O_3 Support

Angelina Barthelmeß,[a] Aude Joviane Wambo Tchatchou,[a] Michael Zimmermann,[a]
Vanessa Trouillet,[b] and Moritz Wolf*[a, c]

This research demonstrates an approach to enhance performance during CO_2 hydrogenation by using carbon nitride (CN)-coated Al_2O_3 composites as a support for cobalt-based catalysts. Unlike conventional fine powdered CN with a typically low surface area, the CN coating on Al_2O_3 enables tuneable porosity and minimizes pressure drop in fixed-bed reactors. Modification of the Al_2O_3 support with CN induced a significantly improved distribution of separately prepared Co_3O_4 nanoparticles. The CN layer interacted strongly with the nanoparticles, preventing aggregation. An enhanced stabilization of nanoparticles was also identified when comparing the Co/CN@Al_2O_3 catalyst with the Co/Al_2O_3 catalyst post reaction. Catalytic tests for CO_2 methanation revealed that Co/CN@Al_2O_3 yields significantly higher CO_2 conversions of up to 63% and a methane selectivity of 94%. In contrast, the Co/Al_2O_3 catalyst exhibits a lower CO_2 conversion of maximum 20% and a methane selectivity of up to 66%. These results illustrate the superior stability and activity of the Co/CN@Al_2O_3 catalyst, which may be linked to a restructuring of the CN into a N-doped carbon (N—C) layer and potential cobalt carbide formation during activation or CO_2 hydrogenation.

1. Introduction

The CO_2 concentration in the atmosphere has increased by about 50% from 280 to 420 ppm since the late 18th century and it is projected to reach 950 ppm or more by the end of this century.[1] The majority of global CO_2 emissions are due to the use of fossil fuels, which in turn account for 80%–90% of the global electricity generation.[1] Since the Paris agreement, the European Union has been targeting a reduction in greenhouse gas emissions of at least 95% until 2050.[2] Renewable energy sources and hydrogen (H_2) alone cannot guarantee the necessary CO_2 reduction, as carbon-intensive industries also emit CO_2. Therefore, CO_2 capture and utilization is a promising strategy for achieving global energy and climate goals. Particularly, the chemical conversion of CO_2 as a C1 resource is increasingly becoming the focus of research.[3,4] As early as the beginning of the 20th century, Paul Sabatier pointed out the potential of CO_2 methanation for recovering carbon resources,[5] which presently experiences a renaissance.[6]

CO_2 hydrogenation with renewable H_2 enables carbon neutral production of energy carriers and chemicals, as well as chemical storage of H_2.[7] The electronic ground state configuration of the CO_2 molecule reveals a low-lying empty shell energy level ($2\pi_u$), and the molecule's electron affinity reaches up to 38 eV, indicating that CO_2 is a strong electron acceptor and a weak electron donor.[8] Catalytic activation of CO_2 can be achieved by transferring electrons to the CO_2 molecule. Depending on the catalyst used, various products can be formed, such as methanol, methane, hydrocarbons, and CO.[9] The most active catalysts for the reduction of CO_2 to methanol and CO are Cu, Pd, and Zn[10–14] while Ni, Rh, and Ru[15–18] are particularly effective in the production of hydrocarbons. Ni is broadly accepted as an affordable methanation catalyst with high intrinsic activity and selectivity,[19–22] but Ni-based catalysts often suffer from deactivation due to sintering and carbon poisoning.[21] Additionally, Weatherbee et al. showed that Co/SiO_2 catalysts may outperform Ni/SiO_2 catalysts in CO_2 hydrogenation.[23] Cobalt-based catalysts are also popular in Fischer–Tropsch synthesis (FTS) due to their high performance in CO hydrogenation. When using CO_2, cobalt based catalysts show a high selectivity for methane (CH_4).[24] Various factors, such as preparation method, metal loading, and support material, influence CO_2 conversion and selectivity for CH_4. The nature of the support material, in particular, has a significant impact on catalytic performance.[21,25]

For CO_2 reduction, we use graphitic carbon nitride (CN)-modified supports since carbon-bonded nitrogen groups, includ-

---

[a] A. Barthelmeß, A. J. Wambo Tchatchou, M. Zimmermann, M. Wolf
Karlsruhe Institute of Technology (KIT), Institute of Catalysis Research and Technology, Hermann-von-Helmholtz-Platz 1 76344, Eggenstein-Leopoldshafen, Germany
E-mail: moritz.wolf@kit.edu

[b] V. Trouillet
Karlsruhe Institute of Technology (KIT), Institute for Applied Materials (IAM) and Karlsruhe Nano Micro Facility, Hermann-von-Helmholtz-Platz 1 76344, Eggenstein-Leopoldshafen, Germany

[c] M. Wolf
Karlsruhe Institute of Technology (KIT), Engler-Bunte-Institut, Engler-Bunte-Ring 1 76131, Karlsruhe, Germany

Supporting information for this article is available on the WWW under https://doi.org/10.1002/cctc.202500506

Table 1. Overview of CN-containing catalysts used in thermocatalytic CO hydrogenation.

Catalyst	Reaction Type	Temp. (°C)	Pressure (bar)	Main Product (selectivity %)	Ref.
Fe/CN	FTS	340	20	C_{5+} (74)	[28]
Co/CN@Al_2O_3	FTS	220	20	C_{5+} (78)	[29]
Co/CN@SBA-15	FTS	230	10	C_{5+} (73)	[30]
Co/CN	FTS	230	20	C_{5+} (70–78)	[31]
Ni/exfoliated CN	Methanation	375	1	CH_4 (>70)	[32]

ing pyridinic, pyrrolic, and graphitic N, have been proposed as active sites for CO_2 reduction.[26] Due to its unique structure, CN promotes electron transfer in supported catalysts, improving the stability of highly dispersed metal particles.[27,28] Although CN is primarily used in photocatalytic and electrocatalytic studies, its beneficial properties have also led to application as a support material in thermocatalytic reactions, particularly in CO (Table 1) and CO_2 hydrogenation (Table 2) and reduction reactions, such as methanation or reverse water–gas shift (RWGS).

The reduction behavior and catalytic activity of cobalt on CN-coated alumina in the FTS demonstrated that the CN modification enhances the dispersion of metallic cobalt species.[29,31] Studies have also shown that Cu-modified CN exhibits high catalytic activity in the selective oxidation of benzene[39] and enhanced CO_2 hydrogenation activity at low temperatures.[37] Park et al. demonstrated that CN consistently enhanced the degree of reduction and agglomeration resistance of metal particles, which in turn increased catalytic activity in FTS. This effect was observed for both Co and Fe-based catalysts.[28,29] However, in the case of the iron catalyst, an in situ phase transition to Hägg carbide additionally enhanced the activity.[28]

The goal of this study is to enhance the interaction between cobalt and its support, as well as to improve the support stability by modification of conventional Al_2O_3 with CN. This modification aims at increasing the overall stability but also the performance of the catalyst. CN was prepared onto high-surface-area Al_2O_3, resulting in the formation of a CN@Al_2O_3 composite material. This composite was then used as the support for a Co-based catalyst via the decoration with separately prepared Co_3O_4 nanoparticles.

2. Results

2.1. Characterization of Co_3O_4 Nanoparticles

X-ray diffraction (XRD) confirms the successful separate preparation of single-phase Co_3O_4 nanoparticles with high crystallinity (Figure 1a). The most prominent peak, corresponding to the (311) crystallographic plane at 36.8°, was selected to determine the crystallite size of 8.3 nm (Figure S1 and Table S1) using the Scherrer equation, which is in agreement with the volume mean size of 8.8 nm according to analysis using transmission electron microscopy (TEM). Further, the analysis exhibits the high dispersibility of the synthesized nanoparticles (Figure 1b) as reported in previous studies.[40–43] The nanoparticles exhibit a distinctive cubic morphology and a narrow size distribution (Figure S2) with a relative standard deviation of 17%. Selected area electron diffraction (SAED) further confirms the crystalline nature of the material, showing well-defined polycrystalline diffraction rings that can be indexed to various planes of the spinel-type Co_3O_4 structure, indicating a high degree of crystallinity (Figure S3).

2.2. Characterization of the Supports and Catalysts

Thermogravimetric analysis (TGA) suggests modification of Al_2O_3 with 30 wt% CN (Figure S4). A larger weight loss due to removal of adsorbed species below 250 °C, such as water, was observed for the unmodified Al_2O_3 due to its hygroscopic nature. For the CN@Al_2O_3 support, the surface is mostly covered by CN resulting a lower fraction of volatile compounds. The morphologies of the supports and catalysts were examined with scanning electron microscopy (SEM, Figure 2). The micrographs reveal distinct differences between the morphology of the external surface of bare Al_2O_3 and the CN@Al_2O_3 composite. Al_2O_3 exhibits a smooth surface characterized by angular structures that form larger particles. In contrast, the CN@Al_2O_3 composite shows a rough, irregular surface that seemingly covers the surface of Al_2O_3 particles, including completely filled cracks. This hints toward a complete and evenly distributed coating with CN, which has been previously described for similar approaches.[29,44,45]

Decoration of the supports with the separately synthesized Co_3O_4 nanoparticles via ultrasonication yields the parent catalysts. In the following, the support and catalyst systems will be referred to as modified (CN@Al_2O_3, Co/CN@Al_2O_3) and unmodified (Al_2O_3, Co/Al_2O_3). The loading of Co was analysed by means of ICP-OES and is similar for both catalysts (Table 3). SEM micrographs of the catalysts recorded using backscattered electron detection (ESB) allow for differentiation between cobalt-rich areas and the support as cobalt atoms have a higher atomic number than aluminum or carbon atoms, resulting in stronger electron scattering and an increased signal intensity or visibly brighter image areas. Hence, the distribution of Co on the catalyst surface can be visualized and investigated.[46] For the unmodified catalyst, an accumulation of Co-rich regions is observed, whereas the modified Co/CN@Al_2O_3 shows a significantly improved distribution (Figures 2c,d and S5). Notably, the nanoparticles show a clear tendency to anchor preferentially on the CN coated areas, while thinly coated or bare Al_2O_3 are seemingly less populated (Figure S6). This preference can be attributed to two major factors. First, the N-rich sites in CN form strong interactions with cobalt particles, enhancing their anchoring and preventing aggregation. Secondly, the electronic properties of CN stabilize cobalt atoms, maintaining uniform distribution.[47] STEM-EDX analysis (Figure S7) further supports this observation by revealing a low-intensity aluminum signal

Table 2. Overview of CN-containing catalysts used in thermocatalytic CO_2 reduction.

Catalyst	Reaction type	Temp. (°C)	Pressure (bar)	Main product (selectivity %)	Ref.
Ni/CN	Methanation	20–500	1	CH_4 (>80)	[33]
Cu/CN	RWGS	20–500	1	CO (n.a.)	[33]
15% Ni/MCN	Methanation	200–500	1	CH_4 (100)	[34]
Ni—Ce/exfoliated CN	Methanation	300	1	CH_4 (100)	[35]
Ni/exfoliated CN	Methanation	300	1	CH_4 (>60)	[35]
Ce—Ni—CN	Methanation	200–400	1	CH_4 (100)	[36]
Cu—N_4 SAC	Methanol synthesis	150	1	CH_3OH (95.5)	[37]
Cu—N_3 SAC	RWGS	150	1	CO (94.3)	[37]
Pd/CN (defect-rich)	Liquid phase/ formic acid formation	30–50	30–70	HCOOH (n.a.)	[38]

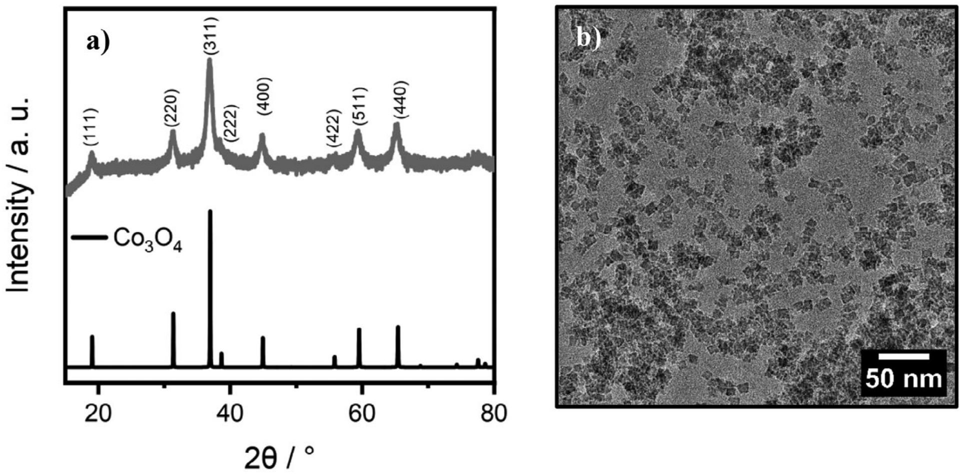

Figure 1. a) XRD pattern with reference pattern for Co_3O_4 and b) TEM micrograph of the synthesized Co_3O_4 nanoparticles.

Table 3. Textural and structural characteristics of support and catalyst samples.

	Al_2O_3	$CN@Al_2O_3$	Co/Al_2O_3	$Co/CN@Al_2O_3$
Cobalt loading (wt%)[a]	–	–	1.7	1.8
Specific surface area (m^2 g^{-1})[b]	175	61	176	40
Total pore volume (cm^3 g^{-1})[c]	0.248	0.079	0.217	0.091
Average pore diameter (nm)[c]	3.651	4.051	3.642	4.013
$d_{V,XRD}$ of Co_3O_4 (nm)[d]	–	–	8.3	
$d_{V,TEM}$ of Co_3O_4 (nm)[e]	–	–	8.8	

[a] Determined by ICP-OES analysis.
[b] Determined by the multi-point BET method.
[c] Determined by the BJH desorption method.
[d] Calculated using Scherer equation from Co_3O_4 (311) plane from XRD.
[e] Calculated using Equation (2).

at the outer surface of the modified catalyst, while nitrogen, carbon, and cobalt signals dominate. This suggests that the outer layer is primarily composed of CN and cobalt species, with only minor contributions from the underlying Al_2O_3 support. Despite the weak Al signal, the Co_3O_4 nanoparticles remain well stabilized and homogeneously distributed within the CN shell, highlighting the structural and chemical robustness of the coating.

The N_2 adsorption-desorption isotherms of the studied samples (Figure 3a) exhibit the typical features of the type IV classification according to IUPAC, which is characteristic for mesoporous materials.[48] Capillary condensation is observed in

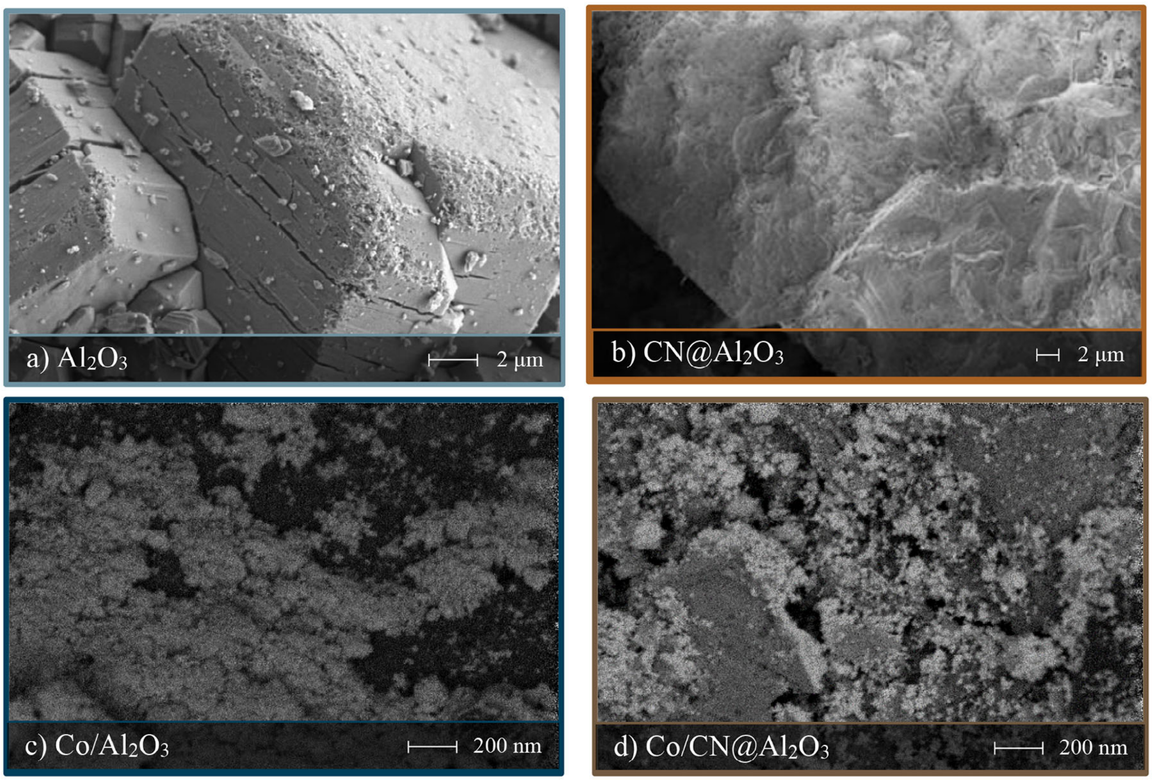

Figure 2. SEM micrographs of a) unmodified Al_2O_3 and b) modified CN@Al_2O_3 support at low resolution (secondary electron images) together with higher resolution images of the corresponding parent catalysts c) Co/Al_2O_3 and d) Co/CN@Al_2O_3 (backscattered electron images).

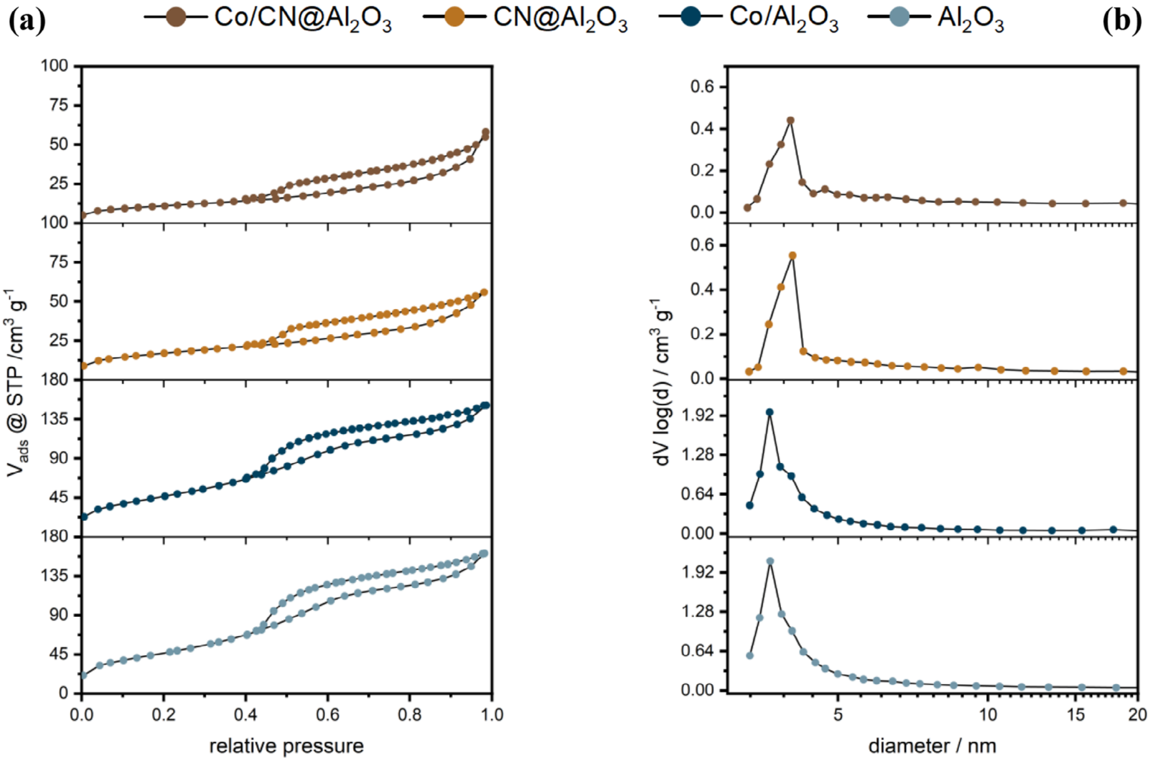

Figure 3. a) Nitrogen adsorption–desorption isotherm and b) incremental pore size distribution of the supports and prepared parent catalysts.

the relative pressure range from 0.45 to 0.97. A detailed analysis of the supports reveals that the coating of Al_2O_3 with CN significantly changes the pore structure in comparison to bare Al_2O_3. Initially, Al_2O_3 shows a hysteresis loop of type H2, indicating complex and irregularly shaped pores. However, following the modification of Al_2O_3 with CN, a shift in hysteresis to type H3 is observed. This can be indicative of slit-shaped pores formed by the aggregation of platelet-shaped particles.[34,35,48] This change reflects the characteristic of pure CN (Figure S8), indicating a complete filling or, more likely, coverage of the Al_2O_3 pore structure by CN.

The BET method suggests a specific surface area of 61 m^2 g^{-1} for CN@Al_2O_3, which is only 35% of the surface area of bare Al_2O_3 (Table 3). Analysis of the pore volume (Figure 3b) using non-local density functional theory (NLDFT) confirms a drastic decrease for CN@Al_2O_3, whereby the average pore size of all samples lies in the mesoporous range of 2–50 nm.[35] It can be assumed that the average pore diameter of the samples is not influenced by the tensile strength effect.[49,50] Comparison of the unmodified Co/Al_2O_3 catalyst with the bare Al_2O_3 suggests an unaltered pore structure by the deposition of nanoparticles on the support. Hence, the nanoparticles are not expected to block pores and, due to their larger size, will mostly be located on the external surface. Interestingly, although both CN@Al_2O_3 and Co/CN@Al_2O_3 exhibit similarly reduced surface areas and pore volumes, the decoration of Co_3O_4 nanoparticles onto the CN-modified support leads to further subtle changes in the isotherm shape and pore size distribution. This suggests that cobalt species interact with the CN matrix, possibly through coordination to nitrogen functionalities or via partial embedding into the CN layer. Such interactions can alter the local structure of the support and influence the dispersion and stabilization of cobalt species. The results demonstrate that the coating of Al_2O_3 with CN mostly covers the Al_2O_3 pore structure while providing altered properties similar to those of bare CN. These results emphasize the effectiveness of the coating process and the successful synthesis of a stable and functional composite material with distributed nanoparticles.

XRD analysis of the parent catalysts features superimposed diffractions of all phases (Figure 4). For CN, a weak, broad peak and a main peak at 12.7° and 27.2° can be assigned to the (100) in-plane repetitive unit of the tri-s-triazine moiety and (022) as the conjugate stacking of the aromatic systems between the layers, respectively.[35] This peak particularly points toward the short-range graphitic structure of CN, as it is a characteristic feature of these materials.[33] Thus, it demonstrates the layer-structural similarities between CN and graphene.[34,51]

The XRD pattern of CN@Al_2O_3 exhibits a superposition of the reflexes of γ-Al_2O_3 and bulk CN. This comes along with a significant reduction in the intensity of the diffraction of the stacking peak, combined with a slight shift toward higher diffraction angles (Figure S9). This trend is also observed for the modified catalyst decorated with Co_3O_4. This indicates that these materials have a smaller distance between the base layers in the CN sheets. This is known for exfoliated CN materials and is due to the fact that thinner layers lead to denser stacking.[51] Hence, the minor shift of only 0.4° is mainly caused by the coating of Al_2O_3 with CN, while the addition of Co_3O_4 nanoparticles hardly affects the crystal structure of CN.[34]

The detailed structural characterization of the CN-modified samples was performed by means of FTIR spectroscopy (Figure 5). The prepared bare CN was compared to the CN@Al_2O_3 composite to identify the influence of Al_2O_3 on the CN structure. The spectra for both, the reference CN and the CN@Al_2O_3, are dominated by features of C-N aromatics, which are characterized via vibrational modes in the fingerprint range of 1241–1650 cm^{-1}. These aromatic compounds have a basic structure based on tri-s-triazine units, as indicated by the distinctive breathing mode at 812 cm^{-1}.[44] The CN@Al_2O_3 composite exhibits a new vibration at 2165 cm^{-1}, which can be assigned to isocyanate.[52] The formation of this additional class of defects is caused by the hydroxyl groups on the surface of alumina, which are identified with a clear broad band at 3600 cm^{-1} for the bare Al_2O_3. These functional groups anchor the amino groups of the transition states and prevent their complete polymerization to CN. [44,52]

Cyano groups are known transition groups from urea to CN and act as electron donors, which are effective anchoring points for nanoparticles or activation processes in the modified support.[53] The broad bands in the range 3061–3414 cm^{-1} can be assigned to N—H and O—H stretching vibrations from adsorbed H_2O.[44,45,54] This demonstrates the presence of incompletely condensed amino functions in all CN materials. The spectrum of the modified catalyst matches with the support, which again confirms, as expected, that decoration with Co_3O_4 does not alter the structural properties. The Co_3O_4 nanoparticles can be identified by the new bands at 664 and 575 cm^{-1}. These bands correspond to the stretching vibrations of Co^{3+} and Co^{2+}, with Co^{3+} being coordinated in a tetrahedral manner, while Co^{2+} exhibits an octahedral environment.[55]

H_2-TPR (Figure 6a) was conducted to investigate the influence of different support systems on the reduction behavior of the Co_3O_4 nanoparticles. Both catalysts exhibit two H_2 consumption peaks at lower temperature due to the stepwise reduction of Co_3O_4 to CoO (α) and subsequently from CoO to Co^0 (β).[56] Deconvolution of the H_2-TPR profiles (Figures S10 and S11, Tables S2 and S3) suggests a lower reduction temperature for Co/Al_2O_3. The difference of approx. 15 °C, when compared to Co/CN@Al_2O_3, can be explained by a Mott-Schottky interaction with CN.[47,57] This interaction delays the reduction slightly, but the accumulation of electrons allows the reduction to proceed more completely and simultaneously. Despite both samples having the same cobalt content and the very same parent Co_3O_4 nanoparticles, variations in peak intensities are observed, which can be attributed to the presence of distinct Co_xO_y species.[36] Following modification, the intensity of the peak in the 400 to 450 °C (β') range is significantly enhanced compared to Co/Al_2O_3 as can be seen from the deconvoluted peaks (Figures S10 and S11, Tables S2 and S3). This suggests that the CN modification reduces the amount cobalt species with weak metal-support interactions and increases those with stronger interactions.[36]

In addition to the cobalt-based reduction peaks, the Co/CN@Al_2O_3 features an additional peak at 537 °C (γ') dominating the overall H_2 consumption. In fact, the major cobalt-based

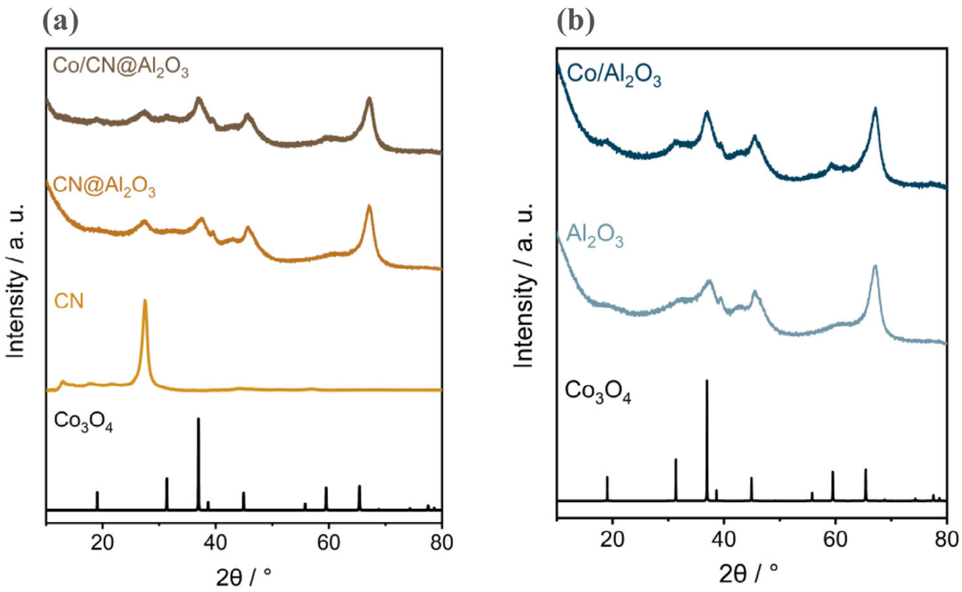

Figure 4. Normalized XRD patterns of a) modified samples and b) unmodified samples as well as the reference patterns for Co_3O_4 and bare CN.

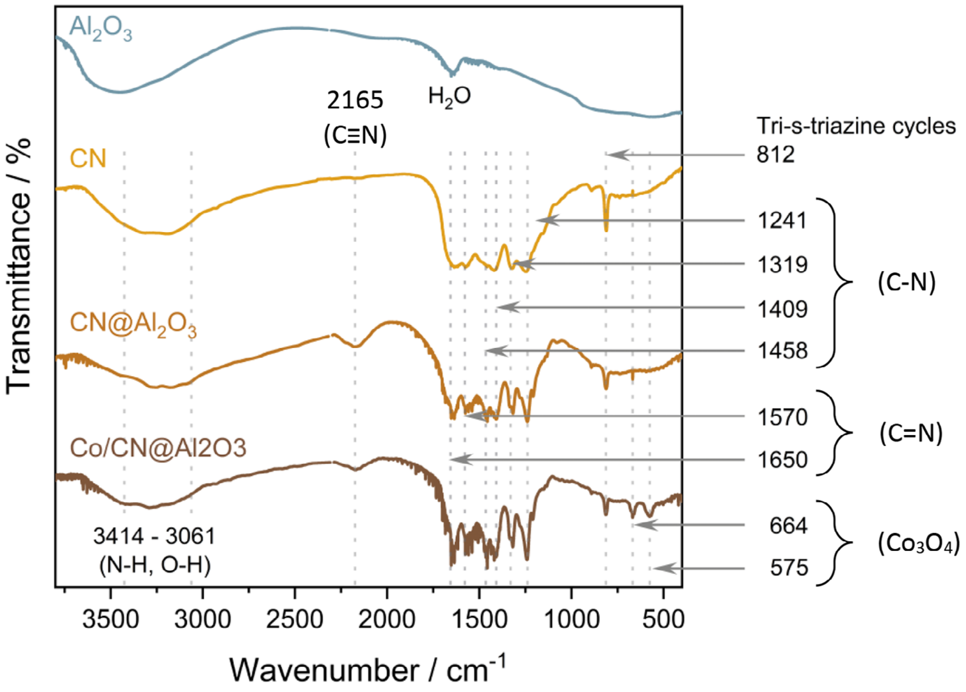

Figure 5. Normalized FTIR spectra of Co/CN@Al_2O_3, CN@Al_2O_3, bare CN, and Al_2O_3.

reduction peak from CoO to Co^0 only represents a shoulder of a more than three times more intense peak. This excessive H_2 consumption must be linked to interaction with CN, such as H_2 induced phase transformation or even decomposition. Interestingly, a similar behavior is observed during H_2-TPR of bare CN with a major peak (γ'') for H_2 consumption at approx. 730 °C, which is in the range of the reported thermochemical stability under H_2 for other CN materials.[58,59] The difference in the peak temperatures of γ' and γ'' of almost 200 °C strongly points toward a lower stability of CN in the presence of cobalt-based nanoparticles.

Hence, the reducible nanoparticles seemingly strongly interact with the CN layers and/or provide activated H_2 in a spillover-type mechanism. The latter might simply accelerate the thermochemical decomposition of CN,[58,59] while interaction of Co^0 with N atoms in the CN might play a major role for the former hypothesis. For example, reduction of nanoparticles along the interlayers of CN may destabilize the structure of the CN causing a shift in the decomposition temperature.[58] Either way, the overall H_2 consumption during TPR is significantly below the expected consumption for full reduction of Co_3O_4 plus complete decomposition of CN.

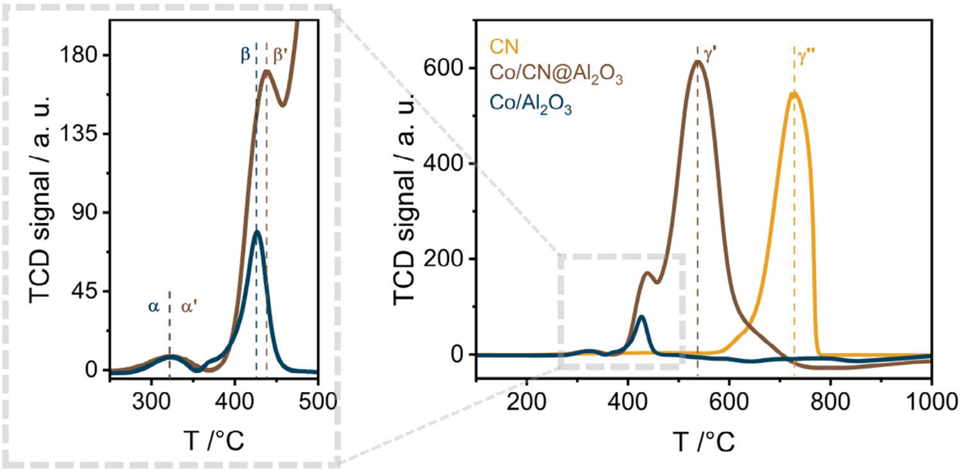

Figure 6. H_2-TPR profiles of the Co/CN@Al_2O_3 and Co/Al_2O_3 catalysts, as well as pure CN. H_2 consumption was acquired in a 5% H_2/Ar atmosphere from 50 °C–1000 °C with a heating ramp of 10 °C min^{-1}.

2.3. Catalytic Performance

CO_2 hydrogenation was conducted in a tubular fixed-bed reactor following in situ catalyst activation in H_2. Based on the results of H_2-TPR as well as the reported reduction behaviors of similar Co_3O_4 nanoparticles on Al_2O_3[60] and less stabilising graphitic carbon support,[42] the catalysts were reduced at 350 °C for 8 h in 40% H_2/Ar. This moderate reduction temperature may also accommodate the low thermochemical stability of CN (Figure 6). Catalytic testing at 5 bar$_g$ using a 4:1 molar inlet ratio of H_2:CO_2 was conducted for temperatures in the range of 300–375 °C with 25 °C intervals and holding time of 2 h each (Figure 7). The

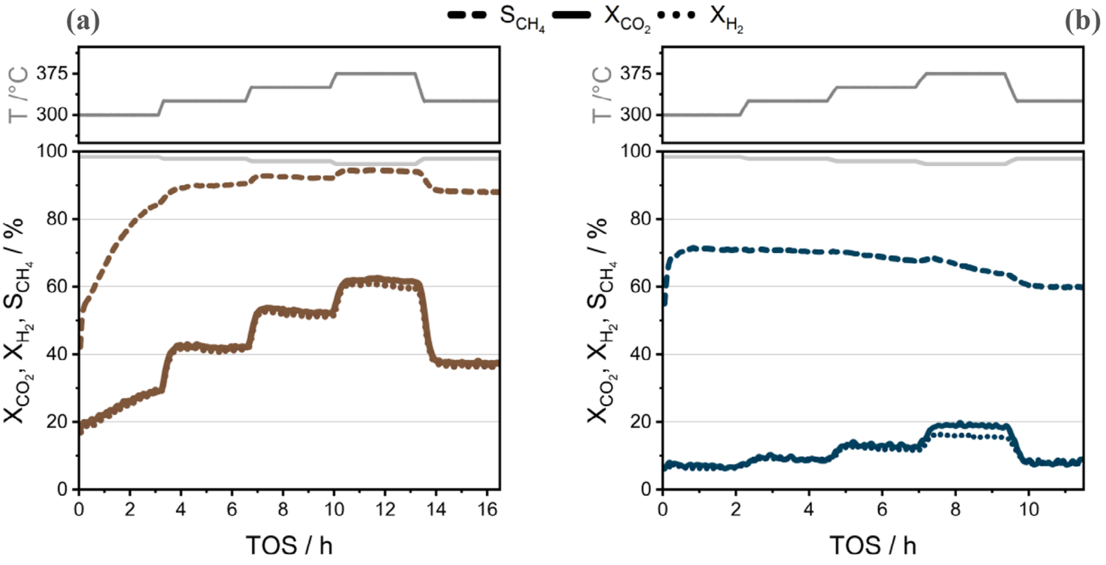

	Co/CN@Al2O3		Co/Al2O3	
T (°C)	X_{CO_2}	S_{CH_4}	X_{CO_2}	S_{CH_4}
300	24.8	72.6	7.0	70.7
325	42.2	89.9	9.5	70.6
350	52.8	92.4	12.9	68.7
375	62.6	94.3	18.9	65.6

Figure 7. H_2 (dotted line), CO_2 conversion (solid line) and CH_4 selectivity (dashed line) at different temperatures for a) Co/CN@Al_2O_3 and b) Co/Al_2O_3 during CO_2 methanation at 300 to 375 °C and 5 bar$_g$ with a H_2:CO_2 inlet ratio of 4:1 and a WHSV of 5000 mL h^{-1} g^{-1}. The light grey solid line represents the equilibrium CO_2 conversion. The tabular overview below summarizes the average CO_2 conversion and CH_4 selectivity at each temperature.

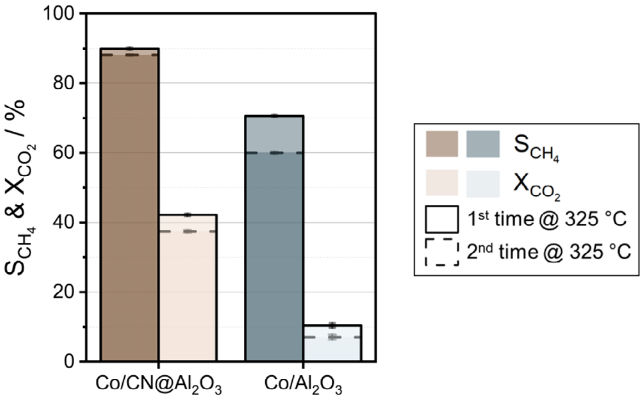

Figure 8. CO_2 conversion ($\mathbf{X_{CO_2}}$) and CH_4 selectivity ($\mathbf{S_{CH_4}}$) of Co/CN@Al_2O_3 (brown) and Co/Al_2O_3 (blue) catalysts at 325 °C before (solid bar) and after (dashed bar) temperature variation.

Co/Al_2O_3 and Co/CN@Al_2O_3 catalysts display a strong influence of the CN modification from the beginning of the catalytic testing.

At the first temperature level (300 °C), the unmodified catalyst achieves a stable CO_2 conversion of 7%, while the CH_4 selectivity rapidly stabilizes at 71%. Contrary, the Co/CN@Al_2O_3 catalyst experiences a strong activation from 20% to 30% conversion of CO_2, which is accompanied by a selectivity switch from 50% to 85% CH_4. Noteworthy, the activation is not complete after the first holding time of 2 h suggesting an even higher potential. This is evidenced when increasing the temperature to 325 °C, which seemingly accelerates the activation process. Both, the CO_2 conversion and the CH_4 selectivity, stabilize at 42% and 90%, respectively, while the Co/Al_2O_3 benchmark seemingly only experiences the expected accelerated kinetics due to the temperature increase without a significant effect on selectivity. During the following temperatures, the Co/CN@Al_2O_3 achieves a maximum CO_2 conversion of approx. 63% and a CH_4 selectivity of 94% at the highest operation temperature of 375 °C. In comparison, the unmodified Co/Al_2O_3 catalyst exhibits a significantly lower efficiency with a maximum CO_2 conversion of 19% at a CH_4 selectivity of 66%. These results emphasise the superior performance of the CN-modified catalyst with stable conversion levels are obtained upon the initial activation period. Contrary, Co/Al_2O_3 operates at low conversion levels, while a decreasing CH_4 selectivity during the holding time at higher temperatures of 350 and particularly 375 °C suggest structural changes in the catalyst. These structural changes may involve the agglomeration of active phases, reducing its surface area or changes in the surface and porosity, which can affect the catalyst efficiency.

To assess the effect of temperature variation, the catalysts were again tested at a final temperature of 325 °C (Figure 8). The Co/Al_2O_3 catalyst exhibited a decrease of the CO_2 conversion from 10% to 7% when compared to the same temperature during the initial temperature profile, representing a decline to approx. one-third of the initial conversion rate. In contrast, Co/CN@Al_2O_3 only showed a slight decrease from 42% to 38%. In addition, the methane selectivity only decreased by 2% in the case of Co/CN@Al_2O_3, while Co/Al_2O_3 showed a change in its former performance, likely due to the altered catalyst surface during the heating phase, causing a lower CH_4 selectivity. Expectedly, this change was accompanied by an increased formation of CO for the unmodified catalyst, which indicates an incipient shift in the reaction mechanism toward RWGS at higher operation temperature. In line, the CO_2 conversion for Co/Al_2O_3 was higher than the H_2 conversion at 375 °C. This behavior was not observed for the modified Co/CN@Al_2O_3 catalyst with an almost equimolar conversion of CO_2 and H_2 throughout the experiment.

The CH_4 productivity of both catalysts visualises the strong boost in activity and selectivity for Co/CN@Al_2O_3 at all temperature levels (Figure 9). It is once again noted, that both catalysts were prepared with the same parent Co_3O_4 nanoparticles and the observed difference is due to the effect of CN on the nanoparticles during reduction and CO_2 hydrogenation. For Co/Al_2O_3, the previously indicated structural changes in the catalyst resulted in an increasing CO and decreasing CH_4 productivity, which becomes more prominent after each temperature increase. In contrast, no significant change in CO productivity is detected for Co/CN@Al_2O_3 after the initial activation period, i.e., even operation at higher temperatures suppressed the RWGS reaction.

2.4. Characterization of the Spent Catalysts

XRD of the spent catalysts (Figure 10) was conducted without a dedicated passivation step before the removal of the catalyst from the reactor. After the reaction, the reactor was cooled to ambient temperature under a flow of argon and then opened to allow diffusion-limited re-oxidation of pyrophoric Co. Hence, re-oxidation of metallic Co is expected to result in a CoO shell with a metallic core.[61] The absence of diffraction peaks of Co_3O_4 in the XRD patterns of the spent catalysts indicates the successful diffusion limited passivation and initial reduction of both catalysts. In line with literature,[61] the absence of strong CoO features suggests a thin oxide layer. Contrary, metallic cobalt peaks are identified at 44.4°, 51.5°, and 75.8°, which can be attributed to the (111), (200), and (220) fcc-Co planes, respectively.

Surprisingly, the XRD pattern of the spent Co/CN@Al_2O_3 catalyst does not feature the CN diffraction of the parent catalyst at 27°, while a new diffraction at 20° becomes evident. The new peak position matches carbon with a limited long-range structure, such as N-doped carbon.[62,63] This observation suggests that CN has undergone a structural change during the reduction or reaction, possibly due to thermal or chemical activation as observed by an increased H_2 consumption at higher temperatures during H_2-TPR. As Co/CN@Al_2O_3 remains functional during catalytic testing (Figure 7) the Co nanoparticles remain sufficiently stabilized and even experience the previously discussed activation. Otherwise, the pattern of the spent Co/CN@Al_2O_3 catalyst resembles the one of the benchmark Co/Al_2O_3 catalyst. More intense, narrow Co peaks for the unmodified catalyst suggest larger crystallite sizes, which represents the strongest deviation between both patterns. This observation suggests sintering of the nanoparticles during reduction and/or catalytic

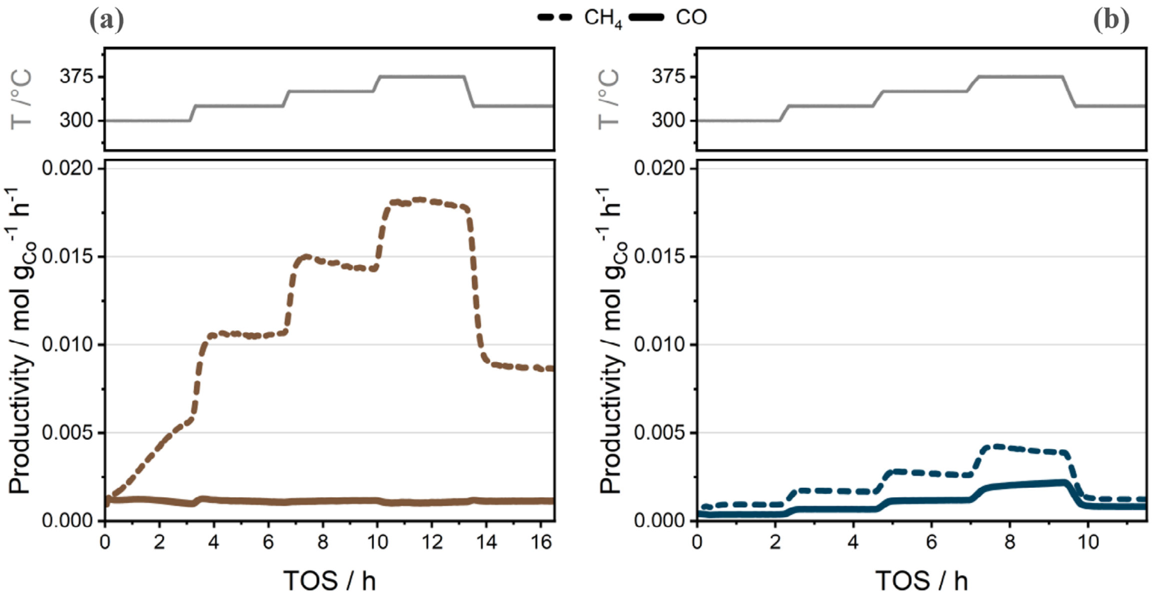

Figure 9. CH_4 (dotted line) and CO productivity (solid line) at different temperatures for a) Co/CN@Al_2O_3 and b) Co/Al_2O_3 during CO_2 methanation at 300 to 375 °C and 5 bar_g with a H_2:CO_2 inlet ratio of 4:1 and a Co loading of 1.8 wt%.

testing,[64] which may explain the decreasing selectivity toward CH_4 at higher temperatures.

To investigate the structural or oxidation state changes induced during treatment of the catalyst and exposure to reaction conditions, the catalysts Co/CN@Al_2O_3 and Co/Al_2O_3 were analyzed by X-ray photoelectron spectroscopy (XPS) before (parent) and after (spent) catalytic testing (Figure 11). For the Co/CN@Al_2O_3 system, the N 1s spectrum (Figure 11a) of the parent sample shows excellent agreement with the characteristic spectral profile of CN. Two dominant features are observed, namely a peak at approx. 398.9 eV, attributed to pyridinic nitrogen, and a second peak at around 400.7 eV, corresponding to tertiary nitrogen (N—$(C)_3$). These two components are indicative of the intact, conjugated structure of CN.[65] After the reaction, the N 1s signal of the spent sample is strongly reduced, approaching the detection limit. This suggests decomposition of the CN structure, leaving behind an amorphous thin carbonaceous layer with low nitrogen content.

This interpretation is further supported by the C 1s spectra. In the Co/CN@Al_2O_3 parent sample, distinct peaks are observed at 285.0 (C—C/C═C), 286.4 (C—N, C—O), and 288.6 eV (C—N_3) (Figure 11b) supporting the presence of CN on the surface. In contrast, the overall intensity of the C 1s spectrum of the spent sample is significantly lower and in particular the peak at 288.6 eV attributed to CN_3 decreased clearly. This structural degradation is also reflected in the quantitative analysis. The total carbon content decreases from approx. 22 at.% in the parent sample to about 11 at.% in the spent sample.

Similar degradation of CN has been previously reported in the literature and linked to the formation of transition metal carbides. Park et al.[28] demonstrated that, when using iron as the active component, the breakdown of the CN matrix facilitated in situ carburization to Fe_5C_2, which was accompanied by a significant increase in catalytic activity. In the present study, the Co 2p region (Figure S12) in the spectrum for Co/CN@Al_2O_3 does not allow for unambiguous identification of a Co_2C phase. The measured cobalt total content is approx. 4 at.%, but it is assumed that any potential carbide formation would be limited to a thin outer shell of the cobalt particles, which could principally be detected together with the further dominant cobalt species. However, such carbide phases typically show a low stability. Potentially formed Co_2C may have decomposed and/or re-oxidized. Additionally, the C 1s spectrum of the spent sample shows no signal in the ~282.0–283.5 eV range (Figure 11b), which would be characteristic of metal–carbon bonds in carbides, further supporting the absence of stable Co_2C species in the analyzed samples.

In the parent sample, cobalt is dominantly present as Co_3O_4, as indicated by the main peak at ~780.0 eV and the characteristic satellite structures at ~785–790 eV. Several fitting procedures are commonly applied to Co 2p spectra. Following the approach applied by Lukhach et al.,[66] the model here considers a main broader peak accompanied by a satellite structure for each Co^{3+} and Co^{2+} oxidation state. Comparison of the different spectra clearly shows that partial reduction of Co_3O_4 occurred under catalytic conditions. After air exposure during post-reaction handling, this reduced phase appears to have stabilized in the form of CoO. A comparison with the unmodified reference catalyst Co/Al_2O_3 reveals that CN modification has no significant influence on the oxidation state or chemical environment of cobalt. In both systems, comparison of the Co 2p spectra of the parent and spent samples lead to similar conclusions: cobalt is present as Co_3O_4 (with some Co^{2+}) before the reaction, and as a mixture of Co_3O_4 and CoO after the reaction.

SEM micrographs of the spent Co/CN@Al_2O_3 catalyst (Figure S13a,c) reveal that the Al_2O_3 surface is still covered by a porous structure, which is most likely a carbonaceous phase as sug-

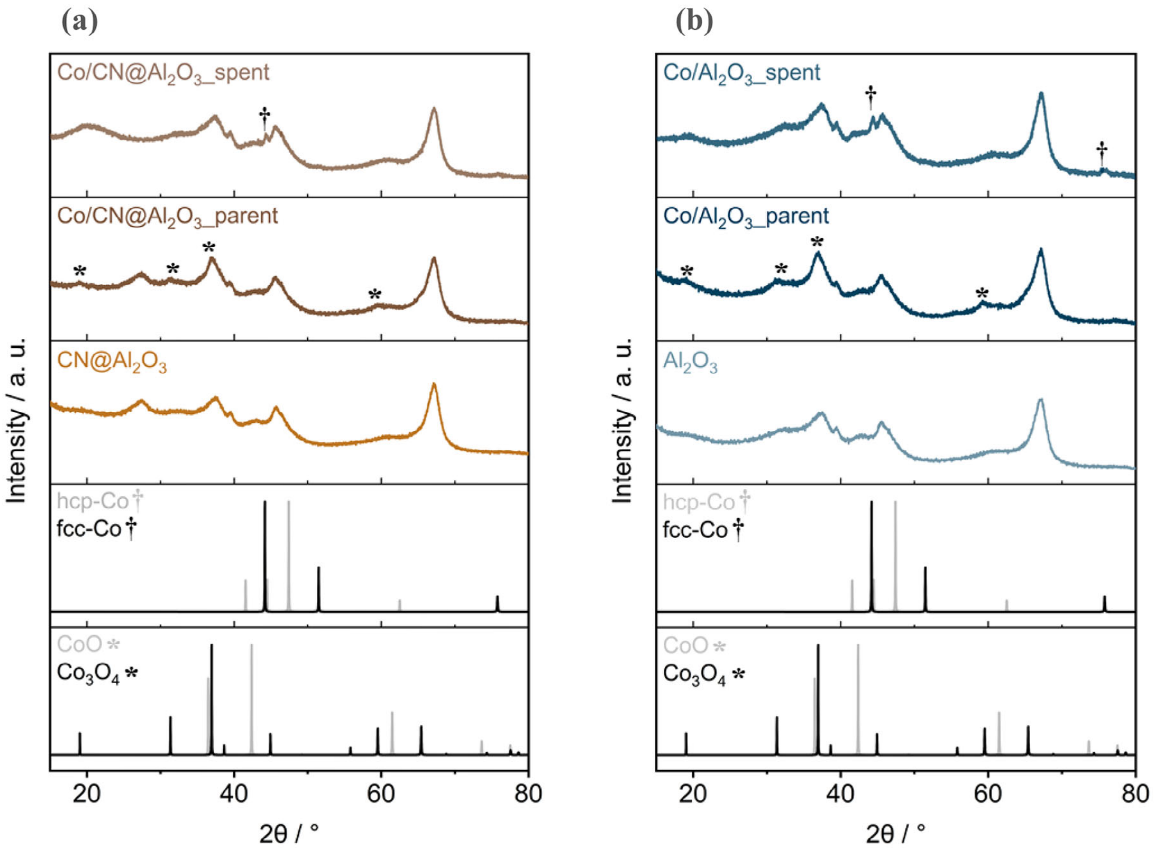

Figure 10. Normalized XRD patterns of a) modified samples and b) unmodified samples before and after CO_2 methanation as well as the reference XRD pattern for Co_3O_4, CoO, fcc-, and hcp-Co.

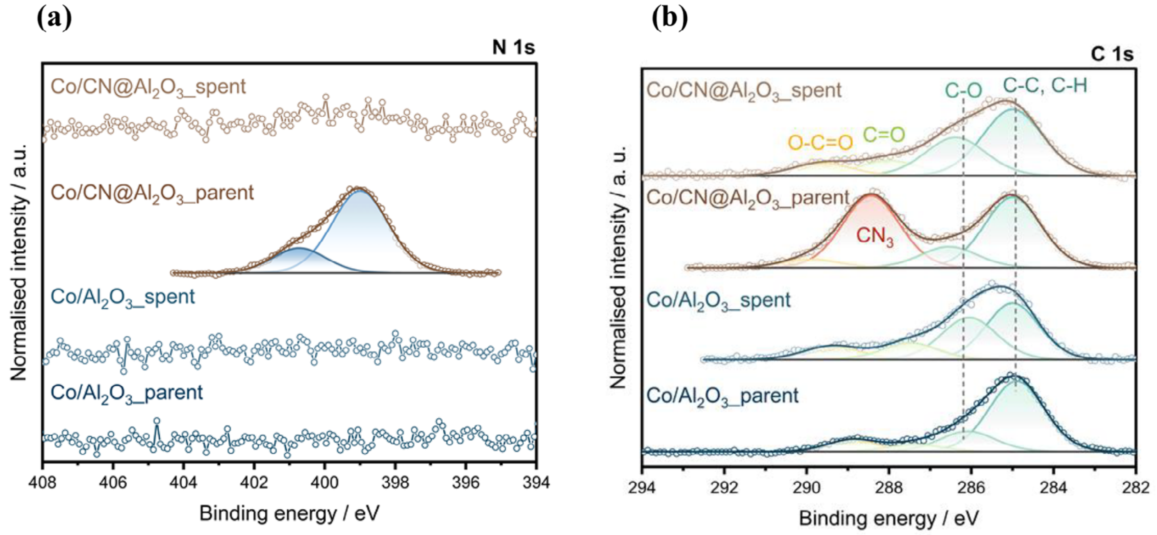

Figure 11. N 1s (a) and C 1s (b) XPS spectra of Co/Al_2O_3 and Co/CN@Al_2O_3 samples in the parent and spent states. All intensities are normalized to the maximum of intensity.

gested by XRD and XPS. In general, the morphological structure of the modified catalyst after CO_2 methanation is similar to the initial coating of CN layer (Figure 2d). Analysis of the distribution of the cobalt phases also shows minor changes. This result is indicative for a stabilized cobalt phase irrespective of the apparent strong structural change of the modified support.

In contrast, SEM analysis of the unmodified catalyst after catalytic testing suggests less stabilization of the nanoparticles (Figure S13b,d), which is in line with an increased crystallite size according to XRD. Here, the inhomogeneous distribution of the cobalt-rich areas on the catalyst surface, which was already apparent after preparation, was even more evident

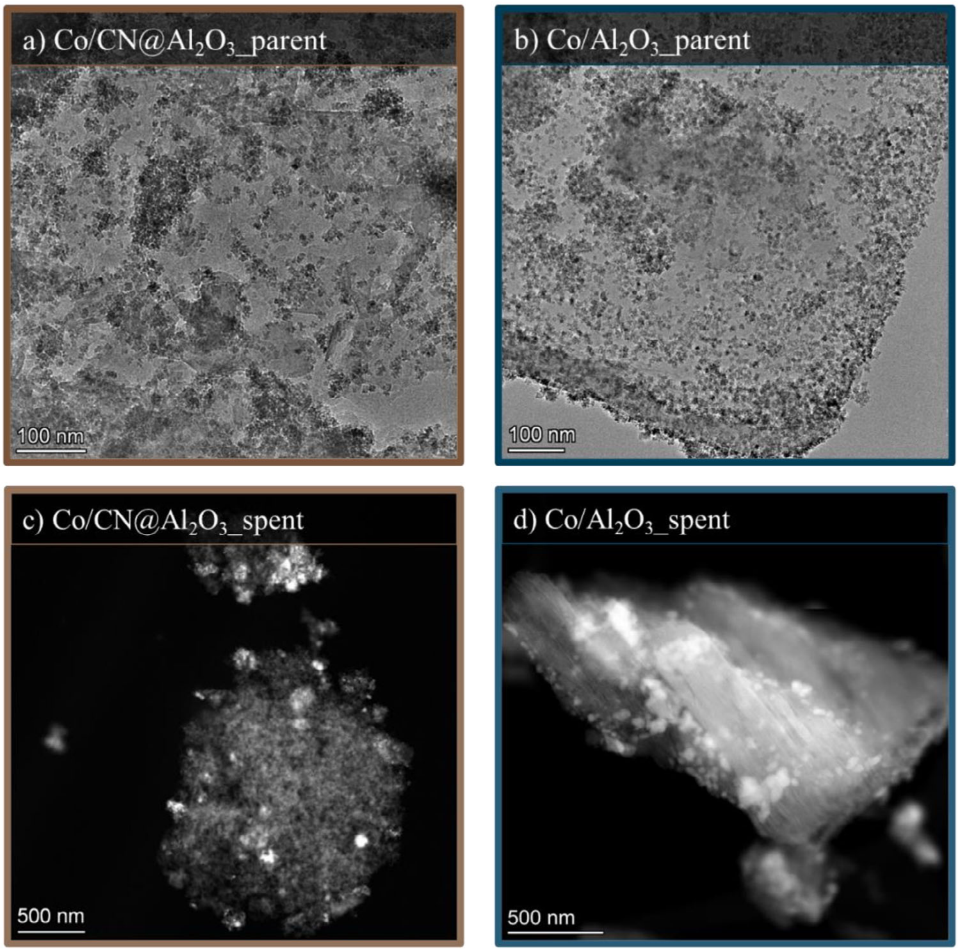

Figure 12. TEM (parent, top) and HAADF STEM (spent, bottom) images of Co/CN@Al_2O_3 a), c) and Co/Al_2O_3 b), d) catalysts before and after catalytic testing.

with a complete absence of individually dispersed nanoparticles. Instead, cobalt is now solely identified in enriched areas, whereby the previously well-distributed nanoparticles form large agglomerates.

This observation is further supported by TEM and HAADF STEM imaging (Figure 12), which reveal distinct structural differences between the two catalysts after testing. The unmodified Co/Al_2O_3 shows extensive particle sintering and coalescence. In contrast, the CN-modified Co/CN@Al_2O_3 catalyst to a large extent retains dispersed nanostructures, as evident from the uniform distribution of small cobalt-containing domains across the carbon-coated surface (Figure S14).

3. Discussion

The results of the conducted studies suggest a strong influence of the CN layer on the nanoparticles, which ranges from enhanced interaction during decoration with Co_3O_4 to a drastic increase in the catalyst stability and performance during CO_2 hydrogenation. H_2-TPR (Figure 6) shows a lowered thermochemical stability of CN in the modified Co/CN@Al_2O_3 catalysts when compared to bare CN, which is either based in hydrogen spill over from the cobalt nanoparticles to CN or strong interaction of nanoparticles with N atoms in the CN structure. Post-run characterization by means of XRD (Figure 10) even reveals the absence of CN diffractions despite of a moderate reduction temperature and CO_2 hydrogenation at $\leq$375 °C, which is approximately the onset temperature of the excessive H_2 consumption during TPR. Park et al.[29] reported similar results for a Co/CN@Al_2O_3 catalyst after FTS. SEM and XRD of the spent Co/CN@Al_2O_3 suggest the formation of a carbonaceous phase with similar morphology on the Al_2O_3 than the parent CN. Despite the decomposition, SEM analyses (Figure S13) confirm that the modified catalyst retains a uniform distribution of cobalt nanoparticles.

In general, Co/CN@Al_2O_3 shows a significantly increased CO_2 conversion (Figure 7), which is further improved during an activation period, and strongly favors methanation over RWGS with a selectivity switch from 50% to 94%. The superior performance of Co/CN@Al_2O_3 could be attributed to several factors. First, CN modification enables an improved distribution during decoration of the support with the separately synthesized Co_3O_4 nanoparticles. In addition, the modification supresses sintering of the cobalt phase when compared to Co/Al_2O_3, which retains the higher activity and methane selectivity. Furthermore, electronic interactions between CN and the active phase could change the charge distribution at the active sites, which improves the selectivity in favor of methane formation.[67] The TPR measurements

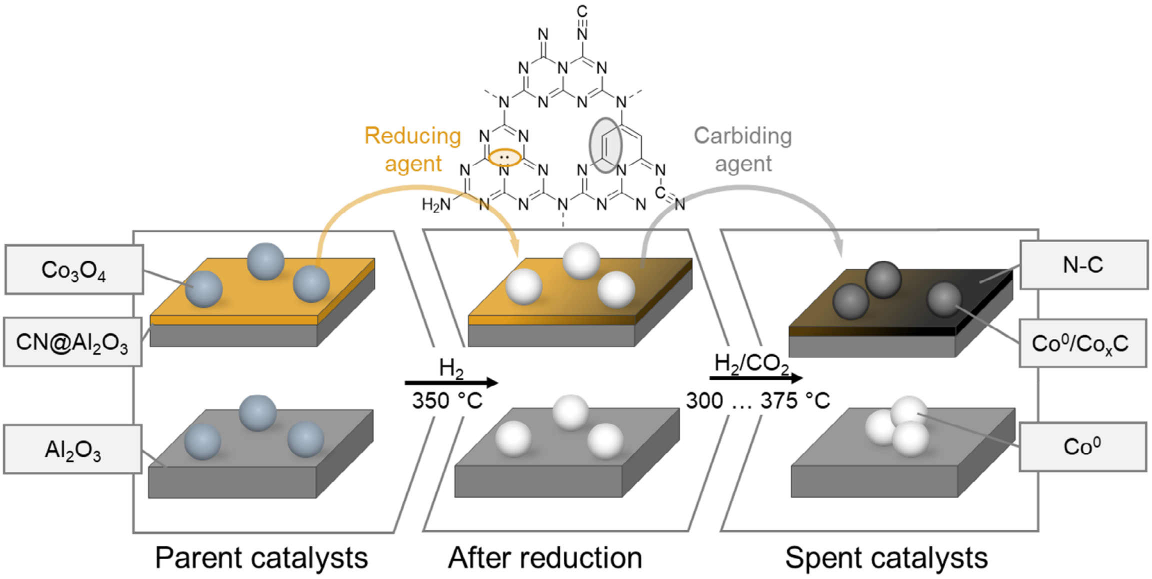

Figure 13. Illustration of the evolution of the catalysts: Co/CN@Al_2O_3 (top) transforms into a well stabilized Co_2C/N-C@Al_2O_3, while Co/Al_2O_3 (bottom) deactivates via particle agglomeration (carburization scheme adapted from Park et al.[28]).

confirmed a stronger interaction between the nanoparticles and the modified support,[36] which ultimately leads to an enhanced reducibility of the nanoparticles.[28,29,68] As incompletely reduced CoO_x can inhibit methane formation, this could also be another decisive factor for the increase in performance as a result of the modification. All of these effects, which mostly increase the availability of Co^0 for catalysis or improve the intrinsic catalytic activity of the catalyst, may explain the boost in activity of Co/CN@Al_2O_3 with a more than two-fold conversion of CO_2 than the benchmark.

The strong activation of Co/CN@Al_2O_3 together with the observed selectivity shift toward almost exclusive production of CH_4 is particularly remarkable. This is most likely linked to the identified transformation of the CN layer, which can be expected to also influence the physicochemical properties of the cobalt phase. The nanoparticles may undergo structural modifications during the reaction (Figure 13), which in this case enhances their catalytic activity. While the initial boost in catalytic performance could be attributed to the synergistic effect between the CN layer and the Co^0 nanoparticles, the partial decomposition of CN during CO_2 hydrogenation conditions may enhance stabilizing electronic effects. Additionally, the CN-derived modification of the catalyst can increase the selectivity for CH_4 by mechanistically enabling or accelerating formate pathways.[36] These interactions could result in a dynamic modification of the support surface, promoting the formation of highly active and selective Co^0.[69–73]

The physical structure of the CN layer remains intact even after undergoing significant changes, namely transformation into a type of carbon layer. The presence of N—C, identifiable in the XRD pattern of the spent modified catalyst,[63] may enhance the intrinsic Co activity and also increase the selectivity toward CO_2 methanation. The incorporation of nitrogen into the carbon matrix likely creates active sites that promote the adsorption and activation of CO_2 and hydrogen, improving overall catalytic performance.[74] Moreover, these nitrogen-induced defects in the carbon structure can alter the electronic properties of cobalt,[75] enhancing charge transfer and lowering the energy barriers for methanation reactions. The N—C layer may also contribute to the stability of the catalyst by preventing sintering and deactivation during extended catalytic cycles.[75] As a result, the synergistic interaction between N—C and cobalt leads to improved catalytic efficiency and longevity. Another plausible explanation is the reorganization of the Co^0 nanoparticles during the activation period, leading to an optimized particle size that facilitates and favors CH_4 formation. Aside from such a structural dependency, an actual phase transformation of Co^0 into a phase with increased intrinsic activity and selectivity may also be at play, namely the formation of Co_xN and Co_xC during the decomposition of CN. Both Co_2C and Co_4N exhibit promising catalytic activity in CO_2 methanation. Since it is already known that CN can promote the formation of Hägg carbide in iron-based FT catalysts, the decomposition of CN as a sacrificial support could similarly activate cobalt-based catalysts.[28] Co_2C, which is considered problematic in the FTS due to its high methane selectivity,[76] shows a strong structural dependency. While spherical particles promote undesirable CH_4 formation, prismatic structures can be tailored to optimise product selectivity.[77] Especially particles smaller than 8 nm favor a high methane yield,[78] highlighting the importance of size and structure control. For Co_4N, no such structural effect is known, yet reports indicate a boost in activity and CH_4 selectivity outperforming metallic cobalt.[70] Mechanistic studies suggest that it facilitates the formation of reactive intermediates.[79]

4. Summary and Outlook

This study presents the preparation and thorough characterization of a Co/CN@Al_2O_3 catalyst that significantly enhances CO_2

hydrogenation performance. The CN coating on Al_2O_3 improves the distribution and stability of cobalt nanoparticles, preventing aggregation and promoting stability. As a result, the catalyst achieves up to 63% CO_2 conversion and 94% methane selectivity, far surpassing the Co/Al_2O_3 catalyst with only 20% CO_2 conversion and 66% methane selectivity. In conclusion, Co/CN@Al_2O_3 shows superior stability and activity, which highlights the potential of CN-coated supports for CO_2 hydrogenation.

The CN layer enhances catalyst performance through strong interactions with cobalt active phase, reducing nanoparticle sintering and improving nanoparticle reducibility, which is crucial for methane formation. Additionally, during the reaction, structural changes in the cobalt phase may lead to the formation of Co_2C or Co_4N, which can further contribute to the increased intrinsic catalytic activity and methane selectivity. Post-reaction analysis suggests that the CN layer undergoes structural transformations, possibly forming N—C, which could also play a crucial role in improving catalytic stability and activity. While the present work presents the fundamental concept and benefits of CN modification during CO_2 hydrogenation using cobalt-based catalysts, the exact mode of the highly active Co/CN@Al_2O_3 catalyst and the fate of the CN modification can be further studied in dedicated in situ studies. In particular, the formation of Co_2C and other potential phases during reaction conditions, and their influence on catalyst performance can be investigated.

5. Experimental Section

5.1. Materials

Cobalt (II) acetate tetrahydrate (98%), neutral γ-alumina (activated, neutral, 100–285 mesh, Brockmann Activity I, Figure S15), and melamine (99.0%) were obtained from Sigma-Aldrich. Benzyl alcohol, acetone, and ethanol were acquired from VWR (Germany). Aqueous ammonia solution (25 wt%) was purchased from Thermo Scientific. All chemicals were used without purification with the exception of ammonia solution, which was diluted with deionized water to a concentration of 20 wt%.

5.2. Synthesis of Co_3O_4 Nanoparticles

The benzyl alcohol route, a solvent-controlled heat treatment without use of surfactants,[40–43] was used to synthesize Co_3O_4 nanoparticles according to literature.[40] In short, 3.2 g of cobalt acetate tetrahydrate were dissolved in 100 mL of benzyl alcohol during magnetic stirring in a round-bottom flask placed in an aluminum block on a hot plate at 70 °C. While maintaining vigorous stirring at 70 °C, 130 mL of 20 vol.% aqueous ammonia solution were added dropwise to the dark purple solution, resulting in the formation of a brown emulsion. When the pH reached 12 according to universal indicator paper, the flask was promptly transferred to a preheated oil bath at 175 °C to enable flash heating of the mixture. The sample was maintained at this temperature for 3 h for aging, then allowed to cool to room temperature under ambient conditions. Subsequently, 100 mL of diethyl ether were added to the mixture and the resulting dispersion was centrifuged in 45 mL bottles at 7830 rpm for 30 min. The centrifugate was redispersed in 15 mL of ethanol using ultrasonication, and 30 mL of acetone was added to destabilise the nanoparticles for the following centrifugation steps. This washing process was repeated once. The nanoparticles were collected and allowed to dry in a fume hood.

5.3. Preparation of Carbon Nitride-Modified Alumina (CN@Al_2O_3)

For the preparation of the CN@Al_2O_3 support,[29] 15.0 g of melamine were dissolved in 350 mL of deionised water in a 500 mL beaker and magnetically stirred at 65 °C for 15 min. A total of 14.0 g of Al_2O_3 was added, followed by an additional 30 min of magnetic stirring. Water was then evaporated by heating to 120 °C using a hot plate and under continuous magnetic stirring. Once the volume was reduced by half, the mixture was transferred into a crucible under continued stirring, which resulted in a white slurry that solidified upon cooling to room temperature. The solid was subjected to a controlled heat treatment in a semi-closed system with an initial drying phase at 120 °C for 2 h, followed by heating at a rate of 2 °C min^{-1} to 500 °C for 2 h to initiate the polymerization, which was followed by polycondensation at 550 °C for another 2 h. The resulting yellow powder was washed with water to remove any residual precursors or NH_3 species and dried at room temperature. Reference CN was prepared by placing 60.0 g melamine in a crucible covered with a lid using the same heating programme as described above.

5.4. Catalyst Preparation

The parent Co/Al_2O_3 and Co/CN@Al_2O_3 catalysts were prepared via decoration of the supports with the separately synthesized Co_3O_4 nanoparticles.[80,81] A desired quantity of Co_3O_4 nanoparticles for a targeted loading of 2.3 wt% was added to 25 mL ethanol, while the corresponding amount of support material was added to 150 mL ethanol in a round-bottom flask. Ultrasonication of both dispersions for 1.5 h resulted in the formation of a stable dispersion for the nanoparticles, while the support was additionally stirred mechanically using an overhead stirrer. The nanoparticle dispersion was added dropwise under continuous ultrasonication to the support slurry. After an additional 2 h of mechanical stirring during ultrasonication, the dispersion was transferred to a rotary evaporator at 80 °C, 900 mbar, and 160 rpm for 2.5 h. Subsequently, the pressure was gradually reduced from 900 to 20 mbar over 2.5 h to ensure complete solvent removal and to collect the parent catalyst. The targeted Co_3O_4 loading of 2.3 wt% corresponds to a Co loading of 1.7 wt%. The catalysts were sieved for use of the 20 to 106 µm fraction in the fixed-bed reactor.

5.5. Characterization Techniques

High-resolution high-angle annular dark-field (HAADF) scanning transmission electron microscopy (STEM) imaging was carried out using Themis 300 transmission electron microscopes (TEM) (Thermofisher Scientific), equipped with a probe aberration corrector and operated at 300 kV. To enhance contrast, nanoparticles were supported on CN@Al_2O_3 prior to analysis. Powders were applied to 300 mesh carbon-coated copper grids by gently covering the film side and removing the excess via dry deposition. Number-based size distributions were determined by measuring the size of more than 80 nanoparticles using the open-source ImageJ software package.[82] The number mean sizes ($d_{n,TEM}$), the volume-mean sizes ($d_{V,TEM}$), and the relative volume-based standard deviations ($\sigma_{V,TEM}$) were calculated based on the measured sizes d_i (Equations 1–3).

$$d_{n,TEM}\,(nm) = \frac{\sum_{i=1}^{N} d_i}{N} \tag{1}$$

$$d_{V,TEM}\,(nm) = \frac{\sum_{i=1}^{N} n_i {d_i}^4}{\sum_{i=1}^{N} n_i {d_i}^3} \tag{2}$$

$$\sigma_{V,\ TEM}\,(\%) = \sqrt{\frac{\sum_{i=1}^{N}\left(n_i {d_i}^3 \left(d_i - d_{V,\ TEM}\right)^2\right)}{\frac{N-1}{N}\sum_{i=1}^{N} n_i {d_i}^3}} \Big/ d_{V,TEM} \times 100 \tag{3}$$

where N is the number of measured particles, and n_i are the particular fractions.

Scanning electron microscopy (SEM) was performed with a Zeiss GeminiSEM 500 with a thermal Schottky field emitter cathode. In addition to an Everhart–Thornley and inlens secondary electrons detectors an in-column energy selective backscattered (ESB) detector was used.

X-ray diffraction (XRD) was conducted using an X'Pert PRO diffractometer (PANalytical) operating at 40 kV and 40 mA using a Ni filtered Cu Kα radiation source ($\lambda = 0.15406$ nm). The patterns were acquired in a 2θ scanning range from 5° to 80° with a step size of 0.017° and a total scan time of 2 h. Obtained XRD patterns were compared to reference patterns of the Powder Diffraction File of the Crystallography Open Database (COD ID; Co_3O_4: 1538531, CoO: 1533087, fcc-Co: 9008466, hcp-Co: 9010967, Al_2O_3: 2015530). As the patterns of Co/Al_2O_3 spent catalysts were affected by residual SiC, these peaks were masked in the diagram to facilitate data analysis and discussion of the results, which leads to occasional gaps within the diffractogram (Figure S16). Diffraction line broadening analysis via the Scherrer equation (Co_3O_4: (311) diffraction) with correction for the instrumental line broadening and a shape factor of 0.9 was applied as a secondary technique to estimate the crystallite size of the nanoparticles via XRD.

For N_2 adsorption–desorption isotherms, the samples were degassed at 250 °C for 12 h. N_2 physisorption was conducted at −196 °C (liquid N_2) using a Quantachrome Nova 2000 instrument. The specific surface areas and pore structure of the materials were approximated according to the Brunauer–Emmett–Teller (BET) and Barrett–Joyner Halenda (BJH) methods, respectively.

FT-IR spectra of the samples were acquired using a Varian 660-IR device after dilution of the samples with KBr powder, grinding and manual tableting. The measurements were obtained by averaging 32 scans within the range of 400 to 4000 cm^{-1} and a resolution of 2 cm^{-1}.

A TGA 2 analyser (Mettler Toledo) was used to examine the weight fraction of CN in CN@Al_2O_3 composites by means of thermogravimetric analysis (TGA). Approx. 2 mg of the sample in a 70 µL alumina crucible were continuously heated from 25 to 1000 °C at a heating rate of 10 °C min^{-1} under a flow of 50 mL min^{-1} of synthetic air. The amount of CN in CN@Al_2O_3 samples was determined as the weight loss after removal of moisture, adsorbed water, and other volatile compounds and the final weight after decomposition/oxidation of the thermally unstable CN, i.e., the weight loss at temperatures exceeding 250 °C.

Cobalt loadings were determined using optical emission spectrometry with inductively coupled plasma (ICP-OES). The measurement was carried out using an Agilent 725 (Agilent Technologies). For this purpose, the catalysts were dissolved in a volumetric 3:1 mixture of HNO_3 and HCl and digested using a microwave. The solutions were atomised in argon plasma gas and the emitted light was measured radially. By analyzing the characteristic wavelength of this light, the concentration of the elements in the solution could be determined.

The catalyst reducibility was assessed using H_2 temperature programmed reduction (H_2-TPR), which was conducted using an AMI-300 (ALTAMIRA) equipped with a thermal conductivity detector (TCD). Volatile organic compounds and water were removed at 200 °C (10 °C min^{-1}) in Ar for 2 h prior to analysis. H_2 consumption from a 5% H_2/Ar gas flow was quantified during a temperature ramp from 50 to 1000 °C with a heating ramp of 10 °C min^{-1}.

XPS measurements were performed using a K-Alpha XPS spectrometer (ThermoFisher Scientific, East Grinstead, UK). For data acquisition and processing, the Thermo Avantage software was used. All samples (parent and spent, with and without CN) were analyzed using a microfocused, monochromated Al Kα X-ray source (400 µm spot size). The K-Alpha charge compensation system was employed during analysis, using electrons of 8 eV energy, and low-energy argon ions to prevent any localized charge build-up. The spectra were fitted with one or more Voigt profiles (BE uncertainty: +0.2 eV) and Scofield sensitivity factors were applied for quantification.[83] All spectra were referenced to the C 1s peak (C—C, C—H) at 285.0 eV binding energy controlled by means of the well-known photoelectron peaks of metallic Cu, Ag, and Au, respectively.

5.6. CO_2 Methanation Experiments

Catalytic CO_2 methanation was assessed in a tubular fixed-bed reactor with an internal diameter of 6.50 mm (Figure S17). Before the experiment, 750.0 mg of the catalyst were diluted with 375.0 mg of SiC, loaded into the isothermal zone of the reactor, and fixated with two quartz wool plugs on both sides. The catalysts were reduced in situ using a 40% H_2/Ar gas flow of 45 mL min^{-1} at 350 °C for 8 h. After this activation process, the system was left to cool to 100 °C under a continuous flow of Ar. A pre-mixed gas mixture (H_2/CO_2/Ar = 72/18/10) was used for CO_2 methanation experiments using a flow rate of 62 mL min^{-1}, which corresponds to a weight hourly spaced velocity (WHSV) of 5000 mL h^{-1} g^{-1}. The catalytic experiments were performed in the temperature range from 300 °C to 375 °C with 2 to 3 h holding times at temperature intervals of 25 °C and a constant pressure of 5 bar_g. A final temperature step at 325 °C was added at the end of the experiment. The effluent gas of the reactor was analysed by an online μ-GC fusion gas analyzer system equipped with TCDs (Inficon).

The catalytic performance of the catalysts was assessed based on the conversion of CO_2 and H_2 (X_{CO_2}, X_{H_2}) as well as selectivity toward CH_4 and CO (S_{CH_4}, S_{CO}), which are calculated according to Equations (4) and (5), respectively.[84] The cobalt-based productivity was calculated based on Equation (6).

$$X_k\,(\%) = \frac{n_{k,in} - n_{k,out}}{n_{k,in}} \cdot 100 \tag{4}$$

$$S_i\,(\%) = \frac{n_{i,out}}{\sum n_{products}} \cdot 100 \tag{5}$$

$$Productivity\ \left(mol\ g_{Co}^{-1}\ h^{-1}\right) = \frac{n_{i,out}}{m_{cat,\ metal}} \tag{6}$$

where, $n_{k,in}$ and $n_{k,out}$ are the molar flow rates of CO_2 or H_2 at the reactor inlet and outlet, respectively. Additionally, $n_{i,out}$ is the molar flow rate of methane or CO at the reactor outlet that can be generated with a given mass of catalyst metal $m_{cat,\ metal}$.

Acknowledgments

The authors gratefully acknowledge financial support by the Helmholtz Research Program "Materials and Technologies for the Energy Transition (MTET), Topic 3: Chemical Energy Carriers". They also would like to acknowledge Dr. Thomas Zevaco (TPR), Armin Lautenbach and Elisabeth Herzinger (ICP-OES), Marion Lenzner (TGA), as well as Nikolaj Aljoscha Slaby, Doreen Neumann-Walter and Dr. Thomas Nicola Otto (N_2-physisorption) for their valuable support in sample characterization. Furthermore, Dr. Ulrich Arnold is acknowledged for providing the laboratory infrastructure for CO_2 hydrogenation experiments. Characterization by electron microscopy and XPS was carried out with the support of the Karlsruhe Nano Micro Facility (KNMFi, www.knmf.kit.edu), a Helmholtz Research Infrastructure at Karlsruhe Institute of Technology (KIT, www.kit.edu).

Open access funding enabled and organized by Projekt DEAL.

Conflict of Interests

The authors declare no conflict of interest.

Data Availability Statement

All the data are openly available on Repo4Cat (https://repository.nfdi4cat.org/) via the link: https://hdl.handle.net/21.11165/4cat/8627-798y.

Keywords: Activation · CO_2 hydrogenation · Cobalt carbide · Cobalt catalyst · Selectivity shift

[1] I. Hussain, G. Tanimu, S. Ahmed, C. U. Aniz, H. Alasiri, K. Alhooshani, *Int. J. Hydrog. Energy* **2023**, *48*, 24663–24696.
[2] V. Nationen, (UN). Paris Agreement. https://unfccc.int/sites/default/files/english_paris_agreement.pdf (last accessed on 27.01.2025).
[3] H. Arakawa, M. Aresta, J. N. Armor, M. A. Barteau, E. J. Beckman, A. T. Bell, J. E. Bercaw, C. Creutz, E. Dinjus, D. A. Dixon, K. Domen, D. L. DuBois, J. Eckert, E. Fujita, D. H. Gibson, W. A. Goddard, D. W. Goodman, J. Keller, G. J. Kubas, H. H. Kung, J. E. Lyons, L. E. Manzer, T. J. Marks, K. Morokuma, K. M. Nicholas, R. Periana, L. Que, J. Rostrup-Nielson, W. M. H. Sachtler, L. D. Schmidt, A. Sen, G. A. Somorjai, P. C. Stair, B. R. Stults, W. Tumas, *Chem. Rev.* **2001**, *101*, 953–996.
[4] A. T. Ashcroft, A. K. Cheetham, M. L. H. Green, P. D. F. Vernon, *Nature* **1991**, *352*, 225–226.
[5] I. Fechete, *C. R. Chim.* **2016**, *19*, 1374–1381.
[6] C. Vogt, M. Monai, G. J. Kramer, B. M. Weckhuysen, *Nat. Catal.* **2019**, *2*, 188–197.
[7] S. Rönsch, J. Schneider, S. Matthischke, M. Schlüter, M. Götz, J. Lefebvre, P. Prabhakaran, S. Bajohr, *Fuel* **2016**, *166*, 276–296.
[8] G. Zhou, H. Liu, Y. Xing, S. Xu, H. Xie, K. Xiong, *J. CO2 Util.* **2018**, *26*, 221–229.
[9] W. Wang, S. Wang, X. Ma, J. Gong, *Chem. Soc. Rev.* **2011**, *40*, 3703.
[10] A. Bansode, A. Urakawa, *J. Catal.* **2014**, *309*, 66–70.
[11] K. C. Waugh, *Catal. Lett.* **2012**, *142*, 1153–1166.
[12] S. G. Jadhav, P. D. Vaidya, B. M. Bhanage, J. B. Joshi, *Chem. Eng. Res. Des.* **2014**, *92*, 2557–2567.
[13] J. Díez-Ramírez, J. L. Valverde, P. Sánchez, F. Dorado, *Catal. Lett.* **2016** *146*, 373–382.
[14] H. Bahruji, M. Bowker, G. Hutchings, N. Dimitratos, P. Wells, E. Gibson, W. Jones, C. Brookes, D. Morgan, G. Lalev, *J. Catal.* **2016**, *343*, 133–146.
[15] J. Gao, Q. Liu, F. Gu, B. Liu, Z. Zhong, F. Su, *RSC Adv.* **2015**, *5*, 22759–22776.
[16] M. A. A. Aziz, A. A. Jalil, S. Triwahyono, A. Ahmad, *Green Chem.* **2015**, *17*, 2647–2663.
[17] T. Bligaard, J. K. Nørskov, S. Dahl, J. Matthiesen, C. H. Christensen, J. Sehested, *J. Catal.* **2004**, *224*, 206–217.
[18] T. B. Shoynkhorova, P. A. Simonov, D. I. Potemkin, P. V. Snytnikov, V. D. Belyaev, A. V. Ishchenko, D. A. Svintsitskiy, V. A. Sobyanin, *Appl. Catal. B: Environ.* **2018**, *237*, 237–244.
[19] K. Ghaib, F.-Z. Ben-Fares, *Renewable Sustainable Energy Rev.* **2018**, *81*, 433–446.
[20] S. Weber, K. L. Abel, R. T. Zimmermann, X. Huang, J. Bremer, L. K. Rihko-Struckmann, D. Batey, S. Cipiccia, J. Titus, D. Poppitz, C. Kübel, K. Sundmacher, R. Gläser, T. L. Sheppard, *Catalysts* **2020**, *10*, 1471.
[21] M. Yusuf, A. S. Farooqi, L. K. Keong, K. Hellgardt, B. Abdullah, *Chem. Eng. Sci.* **2021**, *229*, 116072.
[22] Y. Kim, S. Kwon, Y. Song, K. Na, *J. CO2 Util.* **2020**, *36*, 145–152.
[23] G. D. Weatherbee, C. H. Bartholomew, *J. Catal.* **1984**, *87*, 352–362.
[24] C. G. Visconti, L. Lietti, E. Tronconi, P. Forzatti, R. Zennaro, E. Finocchio, *Appl. Catal. A: Gen.* **2009**, *355*, 61–68.
[25] H. Liu, S. Xu, G. Zhou, K. Xiong, Z. Jiao, S. Wang, *Fuel* **2018**, *217*, 570–576.
[26] J. Lin, Z. Pan, X. Wang, *ACS Sustain. Chem. Eng.* **2014**, *2*, 353–358.
[27] J. H. Lee, J. Ryu, J. Y. Kim, S.-W. Nam, J. H. Han, T.-H. Lim, S. Gautam, K. H. Chae, C. W. Yoon, *J. Mater. Chem. A* **2014**, *2*, 9490.
[28] H. Park, D. H. Youn, J. Y. Kim, W. Y. Kim, Y.o H. Choi, Y. H. Lee, S. H. Choi, J. S. Lee, *ChemCatChem* **2015**, *7*, 3488–3494.
[29] H. Park, K. Y. Kim, D. H. Youn, Y.o H. Choi, W. Y. Kim, J. S. Lee, *ChemCatChem* **2017**, *9*, 4098–4104.
[30] Y. Zhao, S. Huang, C. Liu, Y. Zhang, L. Wang, A. lin, J. Li, *J. Taiwan Inst. Chem. Eng.* **2024**, *156*, 105328.
[31] H. Oliaei Torshizi, A. Nakhaei Pour, A. Mohammadi, Y. Zamani, *New J. Chem.* **2020**, *44*, 6053–6062.
[32] K. N. Ahmad, S. A. Anuar, W. N. R. Wan Isahak, M. I. Rosli, M. A. Yarmo, *ACS Appl. Mater. Interfaces* **2020**, *12*, 7102–7113.
[33] I. S. Pieta, B. Gieroba, G. Kalisz, P. Pieta, R. Nowakowski, M.u. Naushad, A. Rathi, M. B. Gawande, A. Sroka-Bartnicka, R. Zboril, *Ind. Eng. Chem. Res.* **2022**, *61*, 10496–10510.
[34] Z. Refaat, M. E.l Saied, A. O. A. E.l Naga, S. A. Shaban, H. B. Hassan, M. R. Shehata, F. Y. E.l Kady, *Sci. Rep.* **2023**, *13*, 4855.
[35] K. N. Ahmad, W. N. R. Wan Isahak, M. I. Rosli, M. R. Yusop, M. B. Kassim, M. A. Yarmo, *Appl. Surf. Sci.* **2022**, *571*, 151321.
[36] Y. Yu, Y.i M. Chan, Z. Bian, F. Song, J. Wang, Q. Zhong, S. Kawi, *Int. J. Hydrog. Energy* **2018**, *43*, 15191–15204.
[37] T. Yang, X. Mao, Y. Zhang, X. Wu, L.u Wang, M. Chu, C.-W. Pao, S. Yang, Y. Xu, X. Huang, *Nat. Commun.* **2021**, *12*, 6022.
[38] C. Mondelli, B. Puértolas, M. Ackermann, Z. Chen, J. Pérez-Ramírez, *ChemSusChem* **2018**, *11*, 2859–2869.
[39] S. Verma, R. B. Nasir Baig, M. N. Nadagouda, R. S. Varma, *ACS Sustain. Chem. Eng.* **2017**, *5*, 3637–3640.
[40] M. Wolf, N. Fischer, M. Claeys, *Mater. Chem. Phys.* **2018**, *213*, 305–312.
[41] N. Pinna, M. Niederberger, *Angew. Chem. Int. Ed.* **2008**, *47*, 5292–5304.
[42] M. Wolf, N. Fischer, M. Claeys, *Nanoscale Adv.* **2019**, *1*, 2910–2923.
[43] N. Shi, W. Cheng, H. Zhou, T. Fan, M. Niederberger, *Chem. Commun.* **2015**, *51*, 1338–1340.
[44] F.a-T. Li, Y.e Zhao, Q. Wang, X.-J. Wang, Y.-J. Hao, R.-H. Liu, D. Zhao, *J. Hazard. Mater.* **2015**, *283*, 371–381.
[45] S.-H. Lai, Y.-B. Chen, N. Li, H. Su, S. H. Guo, *J. Mater. Sci.: Mater. Electron.* **2018**, *29*, 4509–4516.
[46] A. Garitagoitia Cid, R. Rosenkranz, E. Zschech, *Adv. Eng. Mater.* **2016**, *18*, 185–193.
[47] X.-H. Li, M. Antonietti, *Chem. Soc. Rev.* **2013**, *42*, 6593.
[48] M. Thommes, K. A. Cychosz, *Adsorption* **2014**, *20*, 233–250.
[49] J. C. Groen, L. A. Peffer, J. Pérez-Ramıŕez, *Micropor. Mesopor. Mater.* **2003**, *60*, 1–17.
[50] P. Pang, H. Han, L. Hu, C. Guo, Y. Gao, Y. Xie, *J. Nat. Gas Sci. Eng.* **2021**, *94*, 104060.
[51] P. Niu, L. Zhang, G. Liu, H.-M. Cheng, *Adv. Funct. Mater.* **2012**, *22*, 4763–4770.
[52] Y. Zheng, C. Wei, Q.i An, J. Yu, S. Xu, L. Li, *New J. Chem.* **2021**, *45*, 16750–16759.

[53] J. Zhang, X. Li, J. Zheng, Z. Hu, J. Song, W. Hu, T. Qi, Z. Zhang, *Process Saf. Environ. Prot.* **2024**, *190*, 1105–1113.

[54] R. Romero Toledo, V. Ruiz Santoyo, D. Moncada Sánchez, M. Martinez Rosales, *Nova scientia* **2018**, *10*, 83–99.

[55] A. Karthikeyan, R. Mariappan, R. Bakkiyaraj, E. Krishnamoorthy, *J. Mater. Sci.: Mater. Electron.* **2023**, *34*, 728.

[56] M. Wolf, S. J. Roberts, W. Marquart, E. J. Olivier, N. T. J. Luchters, E. K. Gibson, C. R. A. Catlow, J. H. Neethling, N. Fischer, M. Claeys, *Dalton Trans.* **2019**, *48*, 13858–13868.

[57] Y. Gong, M. Li, H. Li, Y. Wang, *Green Chem.* **2015**, *17*, 715–736.

[58] D. Luo, S. Liu, J. Liu, J. Zhao, C. Miao, J. Ren, *Ind. Eng. Chem. Res.* **2018**, *57*, 11920–11928.

[59] Y. Wang, X. Wang, M. Antonietti, *Angew. Chem., Int. Ed.* **2012**, *124*, 70–92.

[60] M. Wolf, E. K. Gibson, E. J. Olivier, J. H. Neethling, C. R. A. Catlow, N. Fischer, M. Claeys, *ACS Catal.* **2019**, *9*, 4902–4918.

[61] M. Wolf, N. Fischer, M. Claeys, *Catal. Today* **2016**, *275*, 135–140.

[62] X. Teng, C. Ma, C. Ge, M. Yan, J. Yang, Y.e Zhang, P. C. Morais, H. Bi, *J. Mater. Chem. B* **2014**, *2*, 4631.

[63] X. Qian, N. Li, M. Imerhasan, W. Wang, *Colloids Surf. A: Physicochem. Eng. Asp.* **2019**, *573*, 255–261.

[64] G. Garbarino, T. Cavattoni, P. Riani, G. Busca, *Catal. Today* **2020**, *345*, 213–219.

[65] A. F. Pérez-Torres, D. F. Hernández-Barreto, V. Bernal, L. Giraldo, J. C. Moreno-Piraján, E. A. da Silva, M. D.o C. M. Alves, J. Morais, Y. Hernandez, M. T. Cortés, M. A. Macías, *ACS Omega* **2023**, *8*, 47821–47834.

[66] Y. Lykhach, S. Piccinin, T. S. Skála, M. Bertram, N. Tsud, O. Brummel, M. Farnesi Camellone, K. Beranová, A. Neitzel, S. Fabris, K. C. Prince, V. Matolín, J. Libuda, *J. Phys. Chem. Lett.* **2019**, *10*, 6129–6136.

[67] D.-T. Nguyen, C.-C. Nguyen, T.-O. Do, *J. Catal.* **2020**, *392*, 88–96.

[68] Z. Mo, X. Zhu, Z. Jiang, Y. Song, D. Liu, H. Li, X. Yang, Y. She, Y. Lei, S. Yuan, H. Li, L.i Song, Q. Yan, H. Xu, *Appl. Catal. B: Environ.* **2019**, *256*, 117854.

[69] S. Lyu, L.i Wang, J. Zhang, C. Liu, J. Sun, B.o Peng, Y. Wang, K. G. Rappé, Y. Zhang, J. Li, L. Nie, *ACS Catal.* **2018**, *8*, 7787–7798.

[70] R. Razzaq, C. Li, M. Usman, K. Suzuki, S. Zhang, *Chem. Eng. J.* **2015**, *262*, 1090–1098.

[71] Y. Yu, S. Mottaghi-Tabar, M. W. Iqbal, A. Yu, D. S. A. Simakov, *Catal. Today* **2021**, *379*, 250–261.

[72] T. Lin, K. Gong, C. Wang, Y. An, X. Wang, X. Qi, S. Li, Y. Lu, L. Zhong, Y. Sun, *ACS Catal.* **2019**, *9*, 9554–9567.

[73] M. Usman, M. Humayun, M. D. Garba, L. Ullah, Z. Zeb, A. Helal, M. H. Suliman, B. Y. Alfaifi, N. Iqbal, M. Abdinejad, A. A. Tahir, H. Ullah, *Nanomaterials* **2021**, *11*, 2029.

[74] Y. Shang, Y. Ding, P. Zhang, M. Wang, Y. Jia, Y. Xu, Y. Li, K.e Fan, L. Sun, *Chin. J. Catal.* **2022**, *43*, 2405–2413.

[75] Q. Cheng, N. Zhao, S. Lyu, Y.e Tian, F. Gao, L. Dong, Z. Jiang, J. Zhang, N. Tsubaki, X. Li, *Appl. Catal. B: Environ.* **2019**, *248*, 73–83.

[76] M. Claeys, M. E. Dry, E. van Steen, E. du Plessis, P. J. van Berge, A. M. Saib, D. J. Moodley, *J. Catal.* **2014**, *318*, 193–202.

[77] L. Zhong, F. Yu, Y. An, Y. Zhao, Y. Sun, Z. Li, T. Lin, Y. Lin, X. Qi, Y. Dai, L. Gu, J. Hu, S. Jin, Q. Shen, H. Wang, *Nature* **2016**, *538*, 84–87.

[78] Y. Dai, Y. Zhao, T. Lin, S. Li, F. Yu, Y. An, X. Wang, K. Xiao, F. Sun, Z. Jiang, Y. Lu, H. Wang, L. Zhong, Y. Sun, *ACS Catal.* **2019**, *9*, 798–809.

[79] L. Wang, W. Zhang, X. Zheng, Y. Chen, W. Wu, J. Qiu, X. Zhao, X. Zhao, Y. Dai, J. Zeng, *Nat. Energy* **2017**, *2*, 869–876.

[80] M. Wolf, B. K. Mutuma, N. J. Coville, N. Fischer, M. Claeys, *ACS Catal.* **2018**, *8*, 3985–3989.

[81] M. Wolf, N. Fischer, M. Claeys, *J. Catal.* **2019**, *374*, 199–207.

[82] W. S. Rasband, imageJ, https://imagej.net/ij/ (last accessed on 03.11.2025).

[83] J. H. Scofield, *J. Electron Spectrosc. Relat. Phenom.* **1976**, *8*, 129–137.

[84] Y. R. Dias, O. W. Perez-Lopez, *J. Environ. Chem. Eng.* **2021**, *9*, 104629.

Manuscript received: March 21, 2025
Revised manuscript received: July 18, 2025
Accepted manuscript online: August 21, 2025
Version of record online: ■■, ■■